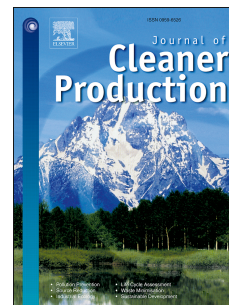


Journal Pre-proof

Thermodynamic evaluation and optimization of supercritical CO₂ Brayton cycle considering recuperator types and designs

Junlin Chen, Keyong Cheng, Xunfeng Li, Xiulan Huai, Hongsheng Dong



PII: S0959-6526(23)01773-0

DOI: <https://doi.org/10.1016/j.jclepro.2023.137615>

Reference: JCLP 137615

To appear in: *Journal of Cleaner Production*

Received Date: 11 March 2023

Revised Date: 29 April 2023

Accepted Date: 28 May 2023

Please cite this article as: Chen J, Cheng K, Li X, Huai X, Dong H, Thermodynamic evaluation and optimization of supercritical CO₂ Brayton cycle considering recuperator types and designs, *Journal of Cleaner Production* (2023), doi: <https://doi.org/10.1016/j.jclepro.2023.137615>.

This is a PDF file of an article that has undergone enhancements after acceptance, such as the addition of a cover page and metadata, and formatting for readability, but it is not yet the definitive version of record. This version will undergo additional copyediting, typesetting and review before it is published in its final form, but we are providing this version to give early visibility of the article. Please note that, during the production process, errors may be discovered which could affect the content, and all legal disclaimers that apply to the journal pertain.

© 2023 Published by Elsevier Ltd.

Junlin Chen: Conceptualization, Methodology, Validation, Writing – original draft. **Keyong Cheng:** Conceptualization, Writing – review& editing. **Xunfeng Li:** Supervision, Writing – review& editing. **Xiulan Huai:** Funding acquisition, Supervision. **Hongsheng Dong:** Investigation, Software, Validation.

Thermodynamic evaluation and optimization of supercritical CO₂ Brayton cycle considering recuperator types and designs

Junlin Chen^{a,b,e}, Keyong Cheng^{a,b,c,d}, Xunfeng Li^{a,b,c,d*}, Xiulan Huai^{a,b,c,d}, Hongsheng Dong^f

^aInstitute of Engineering Thermophysics, Chinese Academy of Sciences, Beijing 100190, China

^bNanjing Institute of Future Energy System, Nanjing 211135, China

^cUniversity of Chinese Academy of Sciences, Nanjing 211135, China

^dUniversity of Chinese Academy of Sciences, Beijing 100049, China

^eKey Laboratory of Ocean Energy Utilization and Energy Conservation of Ministry of Education, Dalian, 116024, China

^fDalian Institute of Chemical Physics, Chinese Academy of Sciences, Dalian 116023, China

* Corresponding author: lixunfeng@iet.cn (Xunfeng Li)

Abstract

The recompression supercritical carbon dioxide Brayton cycle (SCO₂-BC) has great potential for bottoming cycles among future energy conversion systems with comparatively high thermal efficiency. However, the recuperator type selections and optimal designs are a long-standing bottleneck of realizing maximum cycle efficiency and minimum cost. Reasonable collocation of recuperator types remains challenging. In this study, the thermodynamic-economic evaluation and optimization of recompression cycle were performed considering different recuperator types and designs. Printed circuit recuperator channel types include straight, zigzag, S-shaped, and airfoil fins. The design parameters include recuperator enthalpy efficiency and recompression fraction. The results indicate that low-temperature recuperator (LTR) with zigzag channel and high-temperature recuperator (HTR) with zigzag channel exhibit the best comprehensive cycle performance. The cycle thermal efficiency is more sensitive to the HTR enthalpy efficiency compared with the LTR. There is a local inflection point of the recompression fraction where the cycle efficiency is maximum and the exergy loss is minimum. The optimal solution of three-objective optimization considering efficiency, total cost, and exergy loss is more comprehensive than that of the two-objective optimization considering efficiency and cost. In the application of concentrated solar

power, the annual carbon dioxide emission can be directly reduced by 0.43 Gt through this optimization improvement. The results of the current study offer a promising route to high-efficiency and low-cost applications of SCO₂-BC by rational selection of recuperator types and designs.

Keywords: supercritical carbon dioxide recompression Brayton cycle; printed circuit recuperator; thermodynamic and economic evaluation; multi-objective optimization

1. Introduction

One of the most promising schemes would be the supercritical carbon dioxide Brayton cycle (SCO₂-BC) system in the field of clean energy power generation. Compared with the traditional steam-Ranking system, the SCO₂-BC possesses the characteristics of moderate working parameters, high thermal efficiency, simple and compact structure, flexible start-stop, wide temperature ranges, high safety, and cost saving (Guo et al., 2022). As a result of SCO₂'s high density and less compressibility, compression work is significantly reduced. Consequently, compact turbomachines and heat exchangers can be used (Dostal et al., 2006). This cycle can help break the bottleneck of the development of existing power cycle technology. It has broad application prospects in thermal, nuclear, and solar power generation, energy storage system (Deng et al., 2020), coal-fired power plant (Liu et al., 2020), and others (Ahn et al., 2015). Nowadays, it has attracted much more attention as a research hotspot. Several research institutions, e.g., Sandia Nation Laboratory (Iverson et al., 2013), Tokyo Institute of Technology (Utamura et al., 2012), Korean Atomic Energy Research Institute (Al-Sulaiman and Atif, 2015), Xi'an Thermal Power Research Institute (Li et al., 2019), and Institute of Engineering Thermophysics of Chinese Academy of Sciences (Hu et al., 2020), successively performed the experimental loops of the SCO₂-BC and conducted its theoretical studies. It has become a potential way of energy saving and CO₂ resource utilization in the field of power generation, which also has great potential for process improvement and application in terms of cleaner and sustainable production.

To date, different SCO₂ cycle layouts have been proposed and developed, e.g., simple recuperation, recompression, intercooling, and multi-compression cycles. In recent time, the SCO₂ recompression cycle has been the most recognized cycle layout (Tong et al., 2022), which was

proposed to tackle the pinch-point conundrum of the recuperator. It had a very good performance in the nuclear energy system (Dostal et al., 2006), part-load conditions (Yang et al., 2020), and solar power system (Al-Sulaiman and Atif, 2015). Dyreby et al. (Dyreby et al., 2014; Dyreby, 2014) developed a modeling framework to predict the design-point, off-design, and part-load characteristics of different SCO₂-BCs. The results indicate that the recuperator used in the recompression cycle is more balanced.

The aforementioned studies proved that the recompression cycle has a good application prospect. Several studies have shown that recompression cycles are greatly influenced by the performance of recuperators. The research showed that cycle thermal efficiency increased with an increase in the total recuperator conductance (Dyreby, 2014; Neises and Turchi, 2014). In terms of exergy losses, the recuperator effectiveness has a greater effect on the cycle exergy efficiency (Padilla et al., 2015; Wang and He, 2017; Zhao et al., 2016). Besides, the cycle cost is closely related to the recuperators, up to 90% of the cycle cost is in the heat exchangers (Fleming et al., 2013; Rao et al., 2019).

The recuperator, one of the most crucial parts in the SCO₂ cycle, uses a printed circuit heat exchanger (PCHE) on account of its high heat transmission efficiency, small volume, high temperature, and pressure resistance endurance (Lian et al., 2021). To date, researchers have come up with several types of channel patterns. They can be broadly divided into four types: straight, zigzag, S-shaped, and airfoil-fin channels. Chen et al. (Chen et al., 2016) experimentally examined the flow and heat transfer characteristics of a PCHE using a high-temperature helium test device. A comparison was made between zigzag and straight channels in laminar and transition flow states. The results indicated that a zigzag channel has a 2–3 times higher heat transfer coefficient than a straight channel in laminar flow, and the multiple is 1.5–3 times in transition flow. However, the zigzag channel inevitably results in high flow resistance. To improve this problem, researchers developed the S-shaped fin and airfoil fin channels. Tsuzuki et al. (Tsuzuki et al., 2007) proposed S-shaped fin and numerically evaluated its heat-transfer performance. The results indicated that the pressure drop of the zigzag channel was 5 times that of the S-shaped fin with equal thermal–hydraulic performance. Kim et al. (Kim, D.E. et al., 2008) proposed a NACA0020 airfoil fin and found that the pressure drop was reduced to one-twelfth of that in a zigzag channel with the same performance. Moreover, several studies have summarized the correlations of the Nusselt number

(Nu) and friction factor (f) for four different PCHE channel types, which are the basics for PCHE performance analysis and design.

In the system analysis, the PCHE design is crucial for satisfying the requirements of the SCO_2 cycle. Currently, the widespread adoption of Pareto-based multi-objective optimization algorithms promotes the development of cycle design. To optimize the economy of SCO_2 cycle, Zhu et al. (Zhu et al., 2020) developed a new global optimization model using an improved genetic algorithm. In comparison with the conventional unit, the optimized unit reduced its cost by 10.39%. In Zhao et al.'s (Zhao et al., 2016) study, the exergy efficiency and cost per power were optimized based on multi-objective optimization. While Rao et al. (Rao et al., 2019) conducted the optimization with thermal efficiency and total cycle cost. The influences of recuperator's operating conditions are discussed.

The heat source temperature, cycle pressure ratio, inlet temperature of turbine, compressor inlet pressure, pinch-point of the heat exchangers, and recuperator conductance were the common variables in the cycle analysis. However, few studies have been conducted on recuperator types and designs, and multi-objective optimization with more than two objectives is rare. Besides, comparisons between different types of PCHE for SCO_2 -BC have not been carried out in the open literature. The recuperator types and design parameters have a marked impact on the thermodynamic-economic cycle analysis. For example, due to PCHE's high heat-transfer efficiency, capital costs and recuperator volume can be reduced effectively. The low-resistance channels of the PCHE could effectively reduce the pump work of the cycle.

Thus, the multi-objective optimization of the recompression cycle considering different recuperator types and designs was performed in this study. A thermodynamic-economic model was built and verified. The thermodynamic and economic performances of different printed circuit recuperator types were compared, and the recuperator types of low-temperature recuperator (LTR) and high-temperature recuperator (HTR) with the best comprehensive performance were determined. In order to obtain the maximal thermal efficiency, minimum cost and exergy loss, the recuperator enthalpy and recompression fraction were analyzed. Using the non-dominated sorting genetic algorithm (NSGA-II), the two-objective optimization is carried out between thermal efficiency and total cost; then, the three-objectives optimization is performed for efficiency, total cost, and exergy loss. The technique for order preference by similarity to an ideal solution (TOPSIS)

method was used to get an optimal solution.

2. Methods

A representative recompression SCO_2 -BC is illustrated in Fig. 1. The process is as follows: First, SCO_2 flows through the primary heat exchanger (PHE) to reach a high temperature state (5→6). Then, it passes into the turbine, which drives electric generators (6→7). The hot stream is carried through pipes to the HTR (7→8) and LTR (8→9) and becomes a cold stream. At state 9, the cold stream is divided into two streams. One enters the precooler (PC) (9→1) to cool further and is compressed by the main compressor (1→2) to a high-pressure condition. Then, this stream is preheated in the LTR (2→3). The other enters the recompressor (9→10), and the two streams merge at state 4 (10+3→4). After preheating in the HTR (4→5), the SCO_2 stream loops into the PHE.

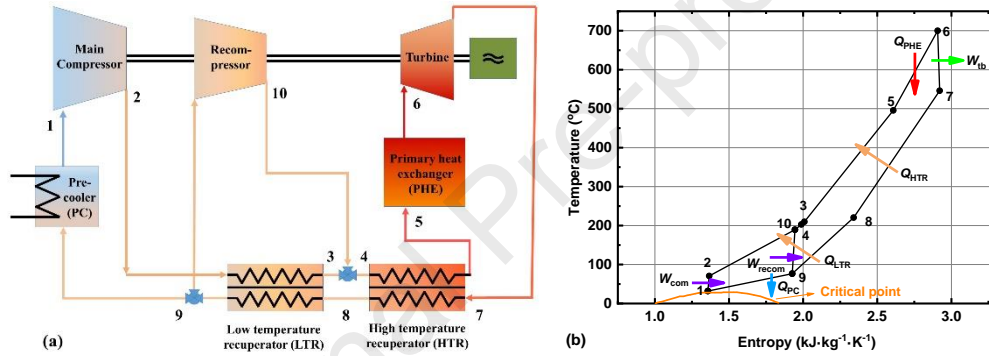


Fig. 1. Flow chart of SCO_2 recompression Brayton cycle.

A computational model of the recompression cycle was built using MATLAB codes. The SCO_2 thermophysical properties of the NIST REFPROP database (Lemmon, 2013) were applied to the program. A thermodynamic model was created based on the one-dimension model and energy balance. The following assumptions were illustrated:

- (1) The recompression cycle condition was the steady state.
- (2) The compression and expansion processes were adiabatic. The efficiencies of the turbine, main compressor, and recompressor were constant, i.e., isentropic efficiency.
- (3) Only the friction loss along the channel of the recuperator, which was the main pressure loss of the recuperator, was considered.
- (4) The pressure loss and heat loss of the pipeline were ignored.
- (5) The pressure loss of the PHE and PC was constant under the same mass flow condition, which was obtained from Dyreby's modeling framework (Dyreby, 2014). In this study, the mass

flow of SCO_2 was $74.968 \text{ kg}\cdot\text{s}^{-1}$, and the pressure losses of the PHE and PC were 245 and 77 kPa, respectively.

2.1 Thermodynamic model

2.1.1 Turbine model

Considering constant isentropic efficiency, the output power of a turbine model is defined as

$$w_{tb,isen} = h_{tb,in} - h_{tb,out,isen}, \quad (1)$$

$$w_{tb} = w_{tb,isen} \cdot \eta_{tb}, \text{ and} \quad (2)$$

$$W_{tb} = m_{\text{CO}_2} \cdot w_{tb} \quad (3)$$

where $h_{tb,in}$ is the inlet specific enthalpy of the turbine; $h_{tb,out,isen}$ is the outlet specific enthalpy of the turbine if the SCO_2 isentropic expands to the outlet pressure; $w_{tb,isen}$ is the isentropic specific work; η_{tb} is the isentropic efficiency; w_{tb} is the specific work; m_{CO_2} is the mass flow rate of SCO_2 , which is constant; W_{tb} is the total output work.

The outlet specific enthalpy ($h_{tb,out}$) is

$$h_{tb,out} = h_{tb,in} - w_{tb} \quad (4)$$

2.1.2 Compressor model

The compressors are also defined as constant isentropic efficiency, and the specific work (w_{comp}) is defined as

$$w_{comp,isen} = h_{comp,out,isen} - h_{comp,in}, \text{ and} \quad (5)$$

$$w_{comp} = w_{comp,isen} / \eta_{comp} \quad (6)$$

where $h_{comp,out,isen}$ is the outlet specific enthalpy if SCO_2 isentropic compresses to the outlet pressure, $h_{comp,in}$ is the inlet specific enthalpy, $w_{comp,isen}$ is the isentropic specific work, and η_{comp} is the isentropic efficiency.

The outlet specific enthalpy of compressor ($h_{comp,out}$) is

$$h_{comp,out} = h_{comp,in} + w_{comp} \quad (7)$$

The total compression power of the compressors is

$$W_{comp} = m_{\text{CO}_2} \cdot (1 - \phi_R) \cdot w_{mc} + m_{\text{CO}_2} \cdot \phi_R \cdot w_{rc} \quad (8)$$

where ϕ_R is the recompression fraction, w_{mc} and w_{rc} are specific work of main compressor and

recompressor, respectively.

2.1.3 PHE and PC model

The heat transfer capacity of PHE (Q_{PHE}) is calculated using

$$Q_{PHE} = m_{CO_2} \cdot (h_{PHE,out} - h_{PHE,in}) \quad (9)$$

where h_{PHX} is the specific enthalpy; subscripts of out and in indicate the outlet and inlet, respectively.

The heat transfer capacity of PC (Q_{PC}) is defined as

$$Q_{PC} = m_{CO_2} \cdot (1 - \phi_R) \cdot (h_{PC,in} - h_{PC,out}) \quad (10)$$

where h_{PC} is the specific enthalpy.

The cycle thermal efficiency (η_{th}) is defined as

$$\eta_{th} = (Q_{PHE} - Q_{PC}) / Q_{PHE} \quad (11)$$

2.1.4 Recuperator model

In the present study, to accurately capture the influence of the SCO_2 variable property, the recuperator was separated into several sub-heat exchangers connected in series along the channel length (Fig. 2) (Guo, 2016). The heat balance calculation for each sub-heat exchanger depended on the outlet and inlet states of the apiece sub-element. The PCHE periodic boundary condition makes it possible to simplify the recuperator model to a single hot channel and a single cold channel. For the recuperator model, initial input parameters were the inlet temperatures of the hot and cold streams, inlet and outlet pressures of the hot and cold streams, enthalpy efficiency, mass flow-rate of single channel, and geometric dimensioning. The number of sub-heat exchangers was set as 400 after the node independence was checked.

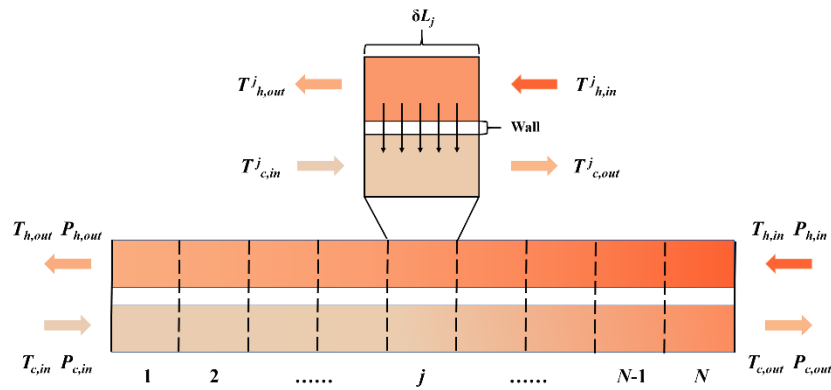


Fig. 2. Segmented counter-flow PCHE model.

The mass flow flux (G) is the mass flow rate per unit area, and the flow-rate of a single channel (m_{ch}) is defined as

$$m_{ch} = G \cdot A_{cs} \quad (1)$$

where A_{cs} is the cross-sectional area of the single channel.

In this study, the heat transfer performance of the recuperator was evaluated by the maximum enthalpy drop of SCO_2 , which differed from the conditional calculation of efficiency based on temperature. The effect of the pinch-point temperature was considered as well. The total heat transfer capacity of model unit (Q_{ch}) is evaluated using the following equation:

$$Q_{ch} = \varepsilon \cdot \Delta h_{max}, \text{ and} \quad (13)$$

$$\Delta h_{max} = \begin{cases} \min\{m_{ch} \cdot (1 - \phi_R) \cdot (h_{c,out}^* - h_{c,in}), m_{ch} \cdot (h_{h,in} - h_{h,out}^*)\} \text{ (For LTR)} \\ \min\{m_{ch} \cdot (h_{c,out}^* - h_{c,in}), m_{ch} \cdot (h_{h,in} - h_{h,out}^*)\} \text{ (For HTR)} \end{cases} \quad (14)$$

where ε is the enthalpy efficiency, $h_{c,out}^*$ is the cold outlet specific enthalpy when temperature is $T_{h,in}$, $h_{c,in}$ is the cold inlet specific enthalpy, $h_{h,in}$ is the hot inlet specific enthalpy, and $h_{h,out}^*$ is the hot outlet specific enthalpy when temperature is $T_{c,in}$.

The heat transfer capacity of sub-channel (δQ_{ch}) is equal for every sub-heat exchanger unit (N), which can be calculated as

$$\delta Q_{ch} = Q_{ch} / N \quad (15)$$

According to the thermal equilibrium and heat transfer relationship of the sub-unit, the channel length of the sub-unit (δL_j) is evaluated as

$$\delta L_j = \delta Q_{ch} / (k_j \cdot Pe \cdot \Delta T_j) \quad (16)$$

where Pe is the perimeter of the cross-section, ΔT_j is the node temperature difference between the cold and hot streams, and k_j is the local comprehensive heat transfer coefficient obtained by:

$$k = \left(\frac{1}{h_h} + \frac{1}{h_c} + \frac{t}{\lambda_m} \right)^{-1} \quad (16)$$

where t is the wall thickness, λ_m is the thermal conductivity of the metal material, which is $16.3 \text{ W} \cdot \text{m}^{-1} \cdot \text{K}^{-1}$, h is the convective heat transfer coefficient defined as

$$h = \lambda_{CO_2} \cdot Nu / D_{hy} \quad (18)$$

where λ_{CO_2} is the thermal conductivity of fluid; Nu is the Nusselt number, which is determined using Reynolds number (Re) and Prandtl number (Pr); and D_{hy} is the channel hydraulic diameter.

The temperature of the $j+1$ node is calculated as (Guo, 2016)

$$m_{ch}(h_{j+1} - h_j) = k \cdot (Pe/1000) \cdot \delta L_j \cdot (T_h^j - T_c^j), \text{ and} \quad (19)$$

$$T^{j+1} = T^j + \frac{h_{j+1} - h_j}{c_p} \quad (20)$$

where c_p is the specific heat of SCO_2 in the j node.

After the element length of the sub-heat exchanger is got, the total pressure drop of the channel (ΔP) is obtained by

$$\Delta P = \sum_{j=1}^N 2 \cdot \frac{f_j}{D_{hy}} \cdot \frac{m_{ch}^2}{\rho A_{cs}} \cdot \delta L_j \quad (21)$$

where f is the Fanning friction factor, and ρ is the density of SCO_2 .

In this study, the following PCHE structures of four different channel types were selected for analysis: straight, zigzag, S-shaped fins, and airfoil fins. The models and size structures of the channel unit are shown in Fig. A1, A3, A5, and A7, respectively. The computational formulas of the hydraulic diameter, cross-sectional area, and perimeter for four different recuperator types are shown in Table 1.

Table 1. Computational formula of the hydraulic diameter, cross-sectional area, and perimeter of four different recuperator types.

	Hydraulic diameter (mm)	Cross- sectional area (mm ²)	Perimeter (mm)
Straight	$D_{hy} = \frac{\pi}{2} \cdot D / (1 + \frac{\pi}{2})$	$A_{cs} = \pi \cdot (\frac{D}{2})^2$	$Pe = \pi \cdot (\frac{D}{2}) + D$
Zigzag	$D_{hy} = \frac{\pi}{2} \cdot D / (1 + \frac{\pi}{2})$	$A_{cs} = \pi \cdot (\frac{D}{2})^2$	$Pe = \pi \cdot (\frac{D}{2}) + D$
S-shape (Rao et al., 2019)	$D_{hy} = \frac{2 \cdot g_f \cdot H_{ch}}{g_f \cdot H_{ch}}$	$A_{cs} = g_f \cdot H_{ch}$	$Pe = 2.18 \cdot (g_f + H_{ch})$
Airfoil (Cui et al., 2018)	$D_{hy} = \frac{4 \cdot (L_b \cdot L_a - S_a) \cdot H_{ch}}{P_a \cdot H_{ch} + 2 \cdot (L_b \cdot L_a - S_a)}$	$A_{cs} = w_{ch} \cdot d_{ch}$	$Pe = \frac{P_a \cdot H_{ch} + 2 \cdot (L_b \cdot L_a - S_a)}{L_b}$

In addition, the correlations of Nu and f for four different channel types were investigated and selected. The specific calculation correlations are expressed in Table 2. In this study, the mass flow-rates of the LTR and HTR were fixed at $330 \text{ kg}\cdot\text{m}^{-2}\cdot\text{s}^{-1}$ to ensure that Re is within the applicable scope of Table 2. The Nu correlation of the airfoil fin was revised based on inlet Re .

Table 2. Correlations of Nu and f for four different recuperator types.

	Nu	f
Straight	$Nu = \frac{(f/2) \cdot (Re - 1000) \cdot Pr}{1 + 12.7 \cdot \sqrt{f/2} (Pr^{2/3} - 1)}$ $2300 \leq Re \leq 10^6, 0.6 \leq Pr \leq 10^5$	$f = \frac{(1.82 \lg Re - 1.64)^{-2}}{4}$ $2300 \leq Re \leq 10^6, 0.6 \leq Pr \leq 10^5$
Zigzag (Ngo et al., 2007)	$Nu = 0.184 Re^{0.629} Pr^{0.317}$ $3500 \leq Re \leq 22000, 0.75 \leq Pr \leq 2.2$	$f = 0.1924 Re^{-0.091}$ $3500 \leq Re \leq 22000, 0.75 \leq Pr \leq 2.2$
S-shape (Ngo et al., 2007)	$Nu = 0.174 Re^{0.593} Pr^{0.43}$ $3500 \leq Re \leq 22000, 0.75 \leq Pr \leq 2.2$	$f = 0.4545 Re^{-0.34}$ $3500 \leq Re \leq 22000, 0.75 \leq Pr \leq 2.2$
Airfoil	$Nu = 0.0318 Re^{0.78} Pr^{0.4}$ $3500 \leq Re \leq 150000,$ $0.6 \leq Pr \leq 0.8$ (Yoon et al., 2014)	$f = 0.08925 \left(\frac{L_b}{L_f}\right)^{-0.252} \left(\frac{W_f}{L_a}\right)^{-0.255} Re^{-0.173} \left(\frac{W_f}{L_a}\right)^{-0.274}$ $8000 \leq Re \leq 100000$ (Chu et al., 2017)

To examine the accurateness of the selected correlations, the theoretical calculation outcomes of the correlations and literature results for each channel were compared. In the comparative analysis of the straight channel (Meshram et al., 2016), the maximum temperature error and maximum pressure drop error along the length were 1.9% and 3.8%, respectively (Fig. A2). As for the zigzag channel (Meshram et al., 2016), the maximum temperature error and pressure drop error along the length were 0.5% and 8.4%, respectively (Fig. A4). The maximum temperature and pressure differences between the inlet and outlet errors of the S-shaped fin channel (Ngo et al., 2007) were 3.41% and 10%, respectively (Fig. A6). While in the comparative analysis of the airfoil fin channel (Cui et al., 2018), the errors of Nu and pressure drop were 1.3% and 9.9%, respectively (Fig. A8). The specific operating parameters of the aforementioned comparisons are shown in the corresponding figures. These errors are permissible in engineering applications. According to the

aforementioned comparison results, Nu correlations and f correlations selected for the four channel types are feasible.

The total channel length (L) is

$$L = \sum_{j=1}^N \delta L_j \quad (22)$$

2.2 Economic model

In the economic analysis, the overall cycle cost includes the compressor, turbine, recuperator, PHE, and PC components costs.

The compressor cost (C_{comp}) and turbine cost (C_{tb}) are functions of their output work based on Carlson's study (Carlson et al., 2017):

$$C_{comp} = 6898 \cdot W_{comp}^{0.7865} \quad (23)$$

$$C_{tb} = 7790 \cdot W_{tb}^{0.6842} \quad (24)$$

The PHE cost (C_{PHE}) and PC cost (C_{PC}) are the functions of the average heat conductance based on Carlson's study (Carlson et al., 2017):

$$C_{PHE} = 3500 \cdot KF_{PHE} \quad (25)$$

$$KF_{PHE} = Q_{PHE} / (T_6 - T_5) \quad (26)$$

$$C_{PC} = 2300 \cdot KF_{PC} \quad (27)$$

$$KF_{PC} = Q_{PC} / (T_9 - T_1) \quad (28)$$

where KF_{PHE} and KF_{PC} are the average heat conductance of the PHE and PC, respectively.

The recuperator cost is only a function of its volume, and the fabrication and interfacing costs are not considered (Yoon et al., 2014). In this study, the recuperator metal density was $7940 \text{ kg} \cdot \text{m}^{-3}$, and the cost of the metal material of the recuperator was $120 \text{ USD} \cdot \text{kg}^{-1}$ (Kim, E.S. et al., 2008). Thus, the cost of the recuperator (C_{recup}) can be calculated as

$$C_{recup} = 7940 \cdot 120 \cdot V \quad (29)$$

where V is the recuperator volume. The recuperator volume calculation formulas for the four channel types are shown in Fig. A1, A3, A5, and A7, respectively.

The total cycle cost (C_{cycle}) can be obtained as

$$C_{cycle} = C_{comp} + C_{tb} + C_{PHE} + C_{PC} + C_{recup} \quad (30)$$

2.3 Exergy loss model

In this study, the exergy efficiency (η_{ex}) was introduced to calculate the exergy loss of PHE and PC. E_L is the exergy loss of different components. E is the exergy value of the different nodes, and is calculated by:

$$E_i = (h_i - h_0) - T_0 \cdot (s_i - s_0) \quad (31)$$

where s denotes the specific entropy of the system node. The subscript 0 represents the environmental status. i is the node in Fig. 1. The ambient temperature (T_0) was 20 °C, and the ambient pressure (P_0) was 101.33 kPa.

The exergy efficiency (η_{ex}) of the heat exchanger can be written by:

$$\eta_{ex} = (E_{c,out} - E_{c,in}) / (E_{h,in} - E_{h,out}) \quad (32)$$

The exergy efficiency of PHE and PC was 80% (Cheng et al., 2021) and 50% (Zhang et al., 2021), respectively. The exergy losses calculation formulas of every component are listed in Table 3.

Table 3. Exergy equation of each component.

Component	Equations
Compressor	$m_{CO_2}(1-\Phi_R)(w_{mc}+E_1-E_2)-E_{L,mc}=0$
Recompressor	$m_{CO_2}\Phi_R(w_{rc}+E_9-E_{10})-E_{L,rc}=0$
Turbine	$m_{CO_2}(E_6-E_7-w_{tb})-E_{L,tb}=0$
LTR	$m_{CO_2}(1-\Phi_R)(E_2-E_3)+m_{CO_2}(E_8-E_9)-E_{L,LTR}=0$
HTR	$m_{CO_2}(E_4+E_7-E_5-E_8)-E_{L,HTR}=0$
PHE	$m_{CO_2}(1-1/\eta_{ex,PHE})(E_5-E_6)-E_{L,PHE}=0$
PC	$m_{CO_2}(1-\eta_{ex,PC})(E_9-E_{10})-E_{L,PC}=0$

2.4 Iteration process

The temperature and pressure states from nodes 1 to 10 were obtained by iterating the aforementioned thermodynamic and economic models. The cycle efficiency, cost, and exergy loss were evaluated. A detailed flowchart of computational course is illustrated in Fig. 3. The input parameters included the performance parameters of the main components of the recompression cycle and recuperator structural parameters. First, the important nodes of the initial temperature and

pressure were initialized, and then, according to the compressor model to obtain T_2 . Next, T_8 was initialized based on turbine model to obtain T_7 . Based on the recuperator model, T_9 , T_3 , P_3 , P_8 , and T_{10} were calculated based on the compressor model. T_4 was evaluated based on the principle of energy conservation. Then, T_8^* , T_5 , T_7 , P_5^* , and P_7^* were calculated according to the recuperator model. We evaluated the values of T_8 and T_8^* until their relative errors are lower than 0.001% and the relative errors of P_5 and P_5^* , P_7 and P_7^* until their relative errors are lower than 0.005%. It can be implied that the thermodynamic iterative process converges. Next, according to the obtained state parameter values of each node, the cost, thermal efficiency, and exergy loss were calculated using the aforementioned formulas. Finally, the Pareto frontier of the optimization solution was obtained based on the NSGA-II.

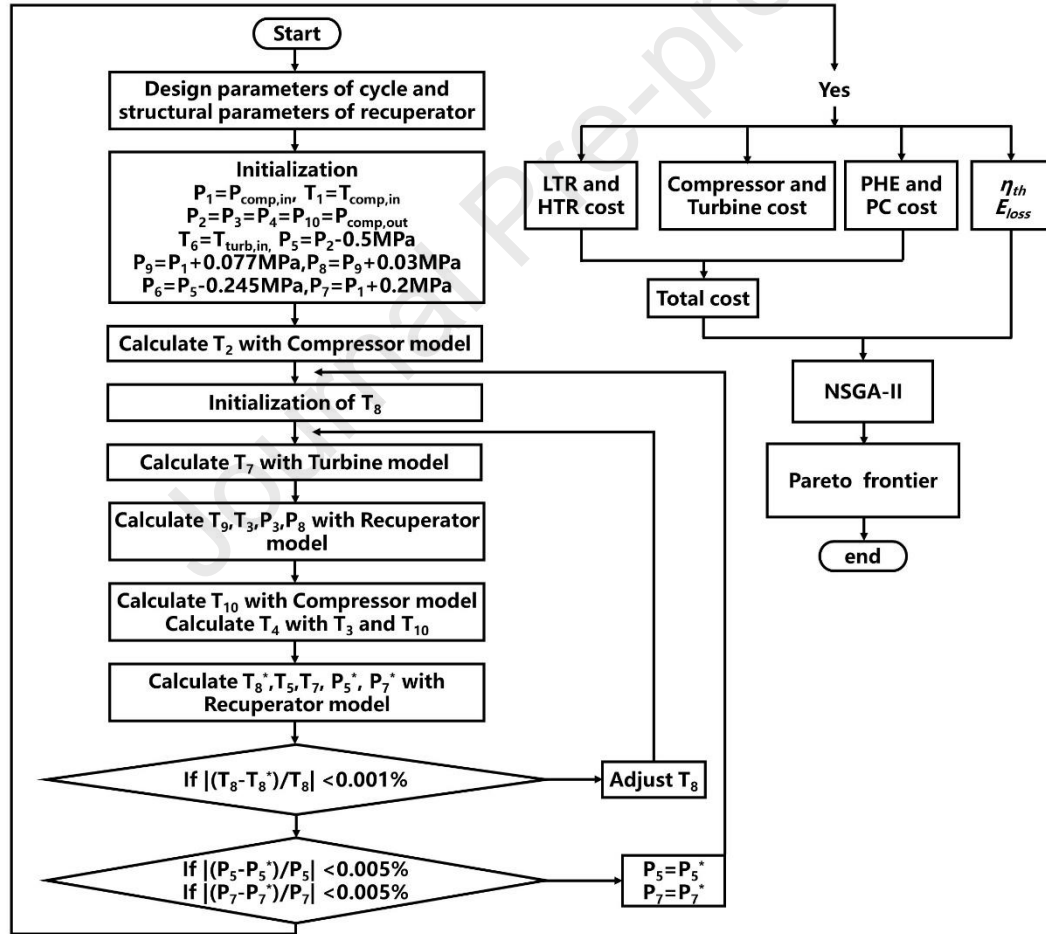


Fig. 3. Flowchart of the iteration process for the thermodynamic-economic model.

2.5 Multi-objective optimization algorithm

In the present study, the most common NSGA-II algorithm was chosen to carry out multi-

objective optimization of cyclic performance. The optimization toolbox used herein was PlatEMO 3.5 (Tian et al., 2017), which can be downloaded from GitHub. It is an evolutionary multi-objective optimization platform that has more than 150 open-source evolutionary algorithms. In PlatEMO, the NSGA-II algorithm is developed to optimize two or three objective functions. Moreover, the multi-objective optimization process is highly integrated. The population size and number of evaluations are required to complete the optimization process on the application module GUI interface. In the optimization process of this study, the population size was 70, and the number of evaluations was 10000.

After obtaining the Pareto optimal frontier curve, it is necessary to analyze and comprehensively evaluate the optimal frontier. The TOPSIS method is a resultful method commonly used in multi-objective decision analysis. Its basic principle is to sort the gap between the evaluation object and the optimal or worst solution. If the gap of optimal solution is minimum, and gap of worst solution is maximum, it is the best solution. The algorithm content is detailed in Rao's (Rao et al., 2019) and Jin's (Jin et al., 2022) studies. SPSSPRO (Suzhou Zhongyan Network Technology Co.), a scientific platform of professional statistical services, was used to get the optimal solution of the optimization results. SPSSPRO can directly perform online data processing, data analysis, and other operations. It can also use various comprehensive evaluation algorithms with easy operation using a GUI interface. In the TOPSIS analysis, the entropy weight method is adopted to obtain the optimal solution. Entropy weights were automatically solved according to entropy information of the algorithm. In the two-objective TOPSIS analysis, the weight of the cycle efficiency and cost were 42.67% and 57.33%, respectively. In the three-objective TOPSIS analysis, the weight of the cycle efficiency, cost, and exergy loss was 34.6%, 30.6%, and 34.8%, respectively.

2.6 Model validation

To examine the accuracy of the recompression cycle thermodynamic model, the cycle efficiency and PHE inlet temperature (T_5) at different turbine inlet temperatures were used to compare the results calculated using Dyreby's modeling framework (Dyreby, 2014). The detailed input parameters are listed in Table 4, where T is temperature, P is pressure, Φ_R is recompression fraction. There is a one-to-one correspondence between the turbine inlet temperature, recompression fraction, and mass flow-rate. The comparison results are displayed in Fig. 4. The maximum error is 2.5% for cycle efficiency and 0.5% for T_5 . These errors may be caused by the deviation in the SCO_2

physical property parameter database and the construction of the algorithm. The comparative results show that the model established in the present study can be performed for further thermodynamic evaluation and multi-objective optimization.

Table 4. Input parameters for the model verification.

Input Parameter	Value	Unit
$T_{tb,in}$	500; 550; 600; 650; 700	°C
$T_{mc,in}$	32	°C
$P_{mc,in}$	7646; 7636; 7628; 7621; 7615	kPa
$P_{mc,out}$	25	MPa
η_{tb}	0.93	
η_{mc}	0.89	
η_{rc}	0.89	
ε_{LTR}	0.95	
ε_{HTR}	0.95	
Φ_R	0.3487; 0.355; 0.3604; 0.3646; 0.3682	
m_{CO_2}	106.94; 96.526; 88.028; 80.954; 74.968	kg/s

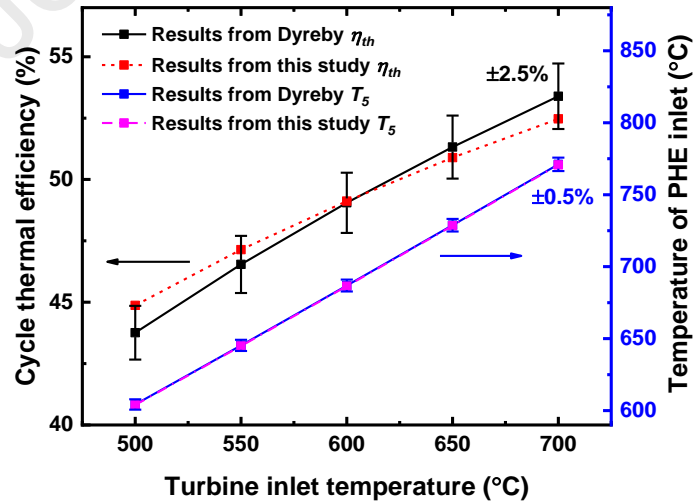


Fig. 4. Comparison of efficiency and T_5 with Dyreby's results (Dyreby, 2014).

3. Thermodynamic and economic analysis

In this section, the cycle performances of four types of channels were compared. Based on this, a combination of HTR and LTR channels with optimal cycle performance was obtained. Then, the influences of the recuperator enthalpy efficiency (ε) and recompression fraction (Φ_R) on cycle efficiency, cost, and exergy loss were discussed.

3.1 Comparison of different channels and the optimal combination

The cycle performances of four different recuperator channels were contrasted under the same conditions: $T_{ib,in}=700$ °C, $P_{mc,in}=7615$ kPa, $\Phi_R=0.3682$, and $m_{CO_2}=74.968$ kg·s⁻¹. The hydraulic diameter was 1.68 mm. The other parameters were consistent (Table 4). The size structures of the four channels are presented in Appendix A. To further obtain the optimal combination of LTR and HTR types, a cycle performance analysis of 16 combinations was performed. The comparison results are listed in Appendix Table A1 and A2. In Table A1 and A2, L and H represent LTR and HTR, respectively. The subscripts st , z , s and af represent the straight, zigzag, S-shaped fin and airfoil fin, respectively. It can be observed that when the LTR and HTR are straight channels, the thermal efficiency is the lowest, and the cost and exergy loss are the highest. This indicates that the performance of the other three recuperator types is superior to that of the traditional straight channel. The zigzag channels have maximal Nu and overall heat transfer coefficient, followed by airfoil fins, S-shaped fins, and straight channels. This lead to the same variation trend of cycle efficiency, and the contrary trend of cost and exergy loss. When the LTR is the type of zigzag, the thermal efficiency is the highest, because the zigzag type possesses the maximal overall heat transfer coefficient. In addition, when the LTR and HTR are zigzag channels, the lowest exergy loss is obtained. This is because the pressure loss of the zigzag channel is the highest, which makes the pressure of P_7 enlarge, resulting in a decrease in the exergy difference between the turbine inlet and outlet. Besides, the total cycle cost is the lowest owing to the volume reduction with a more compact structure. Therefore, the combination of the LTR with the zigzag channel and HTR with the zigzag channel is considered for the recuperator analysis in the following section.

The statistics show that overall installed capacity of concentrated solar power worldwide reached 6.3 GW in 2019 (Merchán et al., 2022). The efficiency of this paper is 4.6% higher than that of steam Rankine cycle (47.94%) (Sharma et al., 2022). If the SCO₂-BC efficiency result of this study replaces the traditional steam Rankine cycle, the annual CO₂ emission can be directly reduced by 0.7 Gt.

3.2 Effect of recuperator enthalpy efficiency ε

Fig. 5(a) and 5(b) show the influences of different ε_{LTR} and ε_{HTR} on the efficiency, cost, and exergy loss, respectively. The cycle efficiency and total cost increase with an increase in the ε . However, the ε_{HTR} impacts the cycle efficiency more than ε_{LTR} . When the enthalpy efficiency increases from 0.7 to 0.99, the cycle efficiency is influenced by HTR increases (from 44.2% to 54.3%), whereas that of LTR increases from 48.3% to 53.6%. It can be concluded that the high ε_{HTR} is more important for cycle efficiency. Nevertheless, the ε_{LTR} is more sensitive to the cycle cost. The main reason is that the LTR is a zigzag channel, and the increase in its efficiency results in an evident increase of volume. Moreover, total cost sharply increases when the efficiency of the LTR and HTR is greater than 0.95, which is the volume increase. The exergy loss of components decreases with an increase in enthalpy efficiency because the greater the heat recovery with an increase in enthalpy efficiency, the more useful energy can be recovered. Further analysis shows that the ε_{HTR} significantly affects the exergy loss. This is partly because the LTR operates at a lower temperature range than the HTR, and the change in enthalpy efficiency leads to a greater floating in heat recovery. In addition, the aforementioned results imply that the optimized ε_{LTR} and ε_{HTR} are required to fulfil higher thermal efficiency, lower exergy loss, and lower overall cost.

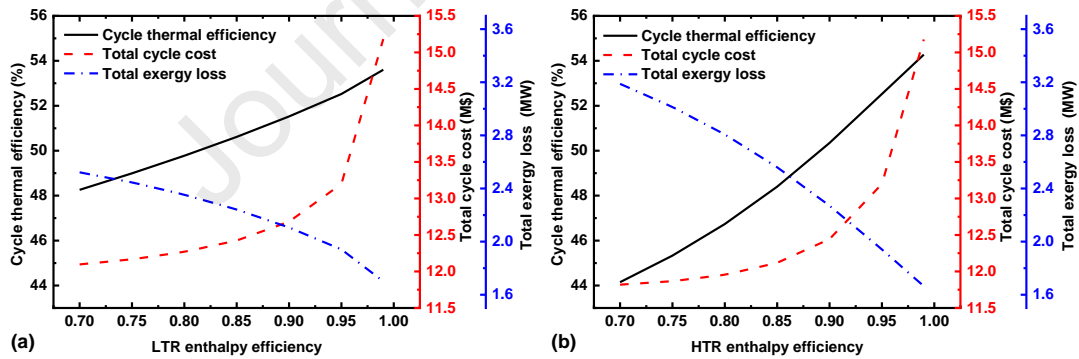


Fig. 5. Influences of ε on the cycle efficiency, cost, and exergy loss: (a) LTR; (b) HTR.

Fig. 6(a) and 6(b) show the impact of different LTR and HTR enthalpy efficiencies, respectively, on the cost of different components. The recuperator cost is mainly affected by the change in enthalpy efficiency and increases with an increase in efficiency. When the enthalpy efficiency is greater than 0.95, the recuperator cost increases sharply because the enthalpy efficiency significantly affects the recuperator volume. Meanwhile, the compressor cost gradually decreases with an increase in enthalpy efficiency. The influence of the HTR enthalpy efficiency on the compressor

cost is evident. With the increase in the enthalpy efficiency, T_9 and T_{10} significantly reduce, which results in a decrease in the compressor power consumption. In particular, the ε_{HTR} significantly impacts the temperature change of T_9 and T_{10} . In summary, enthalpy efficiency negligibly affects the costs of the turbine, PHE, and PC.

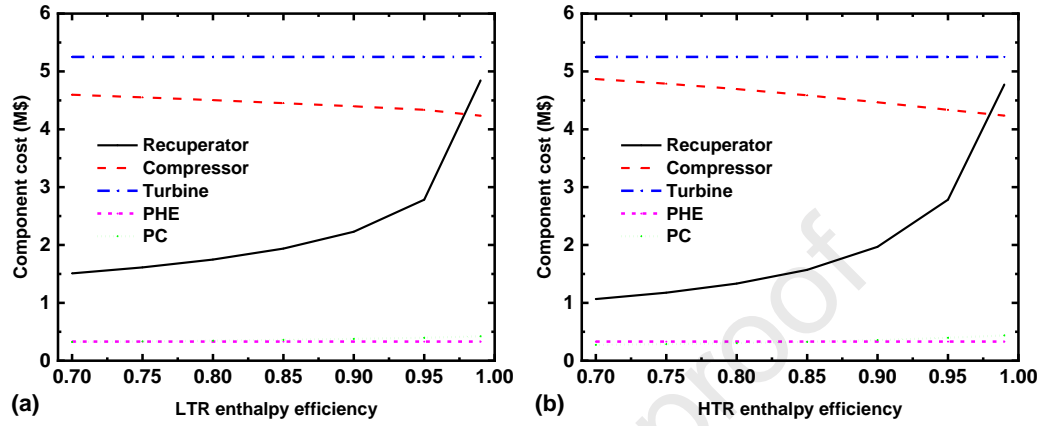


Fig. 6. Influences of ε on the component costs: (a) LTR; (b) HTR.

Fig. 7(a) and 7(b) show the influence of different LTR and HTR enthalpy efficiencies on the exergy loss of different components. The LTR exergy loss is affected by the change in the HTR enthalpy efficiency and gradually decreases with increasing the HTR enthalpy efficiency. The HTR heat recovery increases with an increase in the HTR enthalpy efficiency, thereby reducing the LTR heat load. The LTR enthalpy efficiency remains unchanged, and the LTR exergy loss changes are consistent with those of the heat load. The HTR exergy loss decreases with an increase in the LTR enthalpy efficiency because this increase reduces the heat load of the HTR. The HTR exergy loss first increases and then decreases with increasing the HTR enthalpy efficiency. The increase is related to the heat load, and the decrease is related to the heat exchange area, which sharply increases with an increase in efficiency. The turbine exergy loss decreases with an increase in enthalpy efficiency. When the enthalpy efficiency is greater than 0.95, the turbine exergy loss sharply decreases. The heat exchange area of the recuperator increases when the efficiency is greater than 0.95, and the pressure loss of the recuperator increases. This leads to a significant increase in P_7 , thus resulting in an increase in E_7 , which can be determined by combining the formula in Table 3. In summary, enthalpy efficiency negligibly affects the exergy loss of the compressor, PHE and PC.

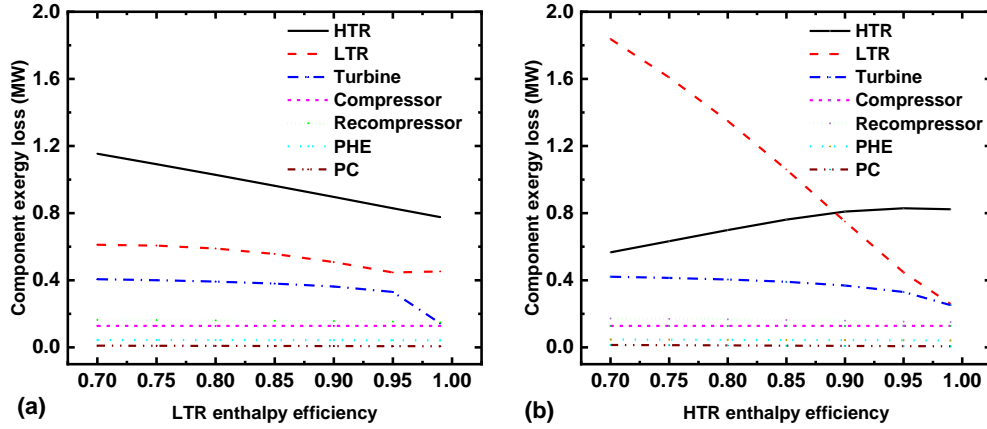


Fig. 7. Effects of ε on the exergy loss of the components: (a) LTR; (b) HTR.

3.3 Effect of recompression fraction Φ_R

Fig. 8 shows the influences of different Φ_R on efficiency, cost, and exergy loss, respectively. When the recompression fraction is 0.33, the cycle efficiency is the highest, the exergy loss is the lowest, and the total cost locally peaks at this point. When the recompression fraction increases from 0.33 to 0.4, the total cycle cost decreases gradually. While the recompression fraction is greater than 0.42, the total cycle cost increases, and its maximum value is higher than the peak value when the recompression fraction is 0.33. This variation is dominated by the recompressor and precooler cost. As the Φ_R increases, recompressor cost increases and precooler cost reduces. The results list that when the recompression fraction is <0.4 , high cycle efficiency and low component exergy loss incur a high cost. Therefore, an optimized recompression fraction is required to achieve high efficiency, low exergy loss, and low cost.

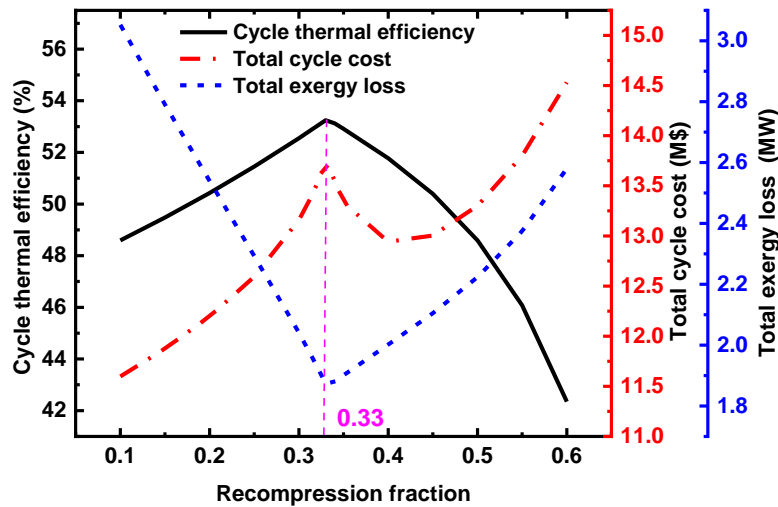


Fig. 8. Influences of Φ_R on the cycle efficiency, cost, and exergy loss.

Fig. 9(a) and 9(b) show the influence of different Φ_R on the cost and exergy loss of each component, respectively. Recompression fraction significantly affects the recuperator cost. When the recompression fraction is 0.33, the total recuperator cost has a maximum peak value. The compressor cost gradually increases with an increase in the recompression fraction. The main reason for this is that much more SCO_2 flowed through the recompressor with increasing recompression fraction, which increases its compression work. The PC cost gradually decreases with an increase in the recompression fraction. The heat transfer quantity of PC decreases with an increase in the recompression fraction owing to the mass that flows through the PC reduces. The cost of PC falls off due to the decrease of the heat transfer area. In Fig. 9(b), as to the exergy losses of the HTR, LTR, and turbine, an inflection point exists when the recompression fraction is 0.33. The LTR exergy loss gradually increases with an increase in recompression fraction, whereas the HTR exergy loss exhibits the opposite trend. This is due to the fact that with increasing recompression fraction, the heat recovery quantity by LTR increases, whereas the heat recovery through HTR decreases. Under the condition of invariable efficiency, the exergy loss changes with the variation in the heat recovery quantity. Moreover, when the recompression fraction is 0.33, the turbine exergy loss is the lowest, which implies that it can do the most useful work. With an increase in the recompression fraction, the mass of SCO_2 flowing into the recompressor increases, whereas the mass in the main compressor decreases. This leads to a decrease in the exergy loss of the main compressor with an increase in the recompression fraction, whereas the exergy loss of the recompressor is inverse. This conclusion can be deduced by combining the relevant calculation formulae presented in Table 3.

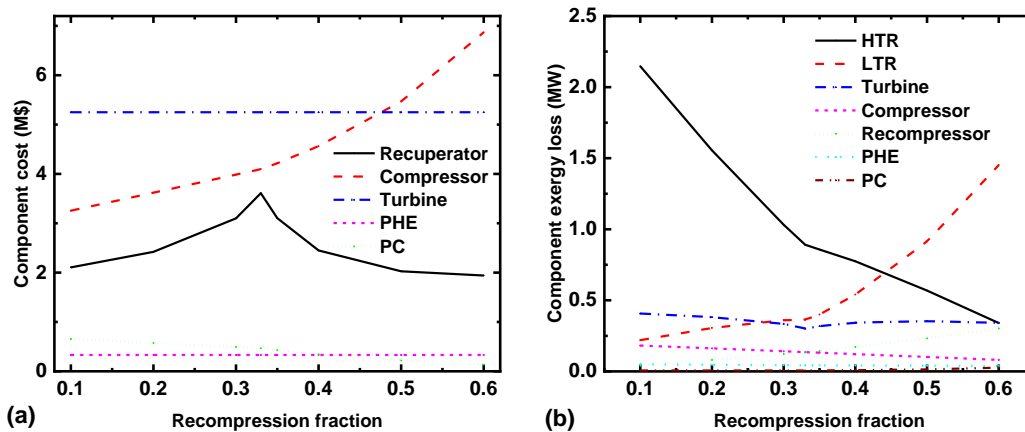


Fig. 9. Influences of Φ_R on the (a) component cost and (b) component exergy loss.

4. Multi-objective optimization

The aforementioned consequences state that the cycle efficiency, cycle cost, and exergy loss are significantly affected by the recuperator enthalpy efficiency and recompression fraction. However, they are in a mutually restrictive relationship. Thus, multi-objective optimization was executed to balance the relationship between them, and to obtain the optimal cycle performance. In the optimization of this section, the recompression fraction varied from 0.2 to 0.5, and the enthalpy efficiency of the LTR and HTR varied from 0.8 to 0.96. The other parameters were the same as previous ones.

4.1 Two-objective optimization

Fig. 10 shows the Pareto frontier curve of the two-objective optimization between cycle efficiency and cost. Five typical points were labeled based on different decisions. The target values corresponding to these five points and corresponding parameter values are listed in Table 5. As shown in Fig. 10, within the selection range of optimization parameters, the value of cycle efficiency ranges from 44.50% to 53.77%, and the total cost ranges from M\$10.71 to M\$14.50. The maximum cycle efficiency is at point E, while the cost is the highest. The lowest cycle efficiency is at point A, where the cost is the lowest. The TOPSIS optimal solution is point C, where the cycle efficiency is 49.37% and the cycle cost is M\$11.58. As shown in Table 5, when the three optimization parameters (ϵ_{LTR} , ϵ_{LTR} and Φ_R) exhibit the lowest values, the corresponding case refers to point A. When the enthalpy efficiency is the highest and the recompression fraction is close to 0.33, the corresponding case is point E. Point C corresponds to the TOPSIS optimal solution, indicating that the HTR should maintain high enthalpy efficiency.

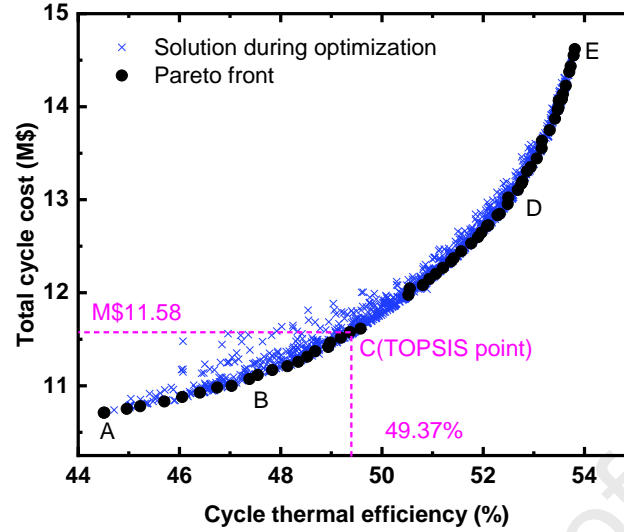


Fig. 10. Pareto frontier curve of the two-objective optimization between cycle efficiency and cost.

Table 5. Five typical points and corresponding parameter values with regard to the Pareto frontier of two objectives.

Point	Decision variables			Two objectives	
	Φ_R	ϵ_{LTR}	ϵ_{HTR}	$\eta_{th}(\%)$	$C_{cycle}(\text{M\$})$
A	0.2	0.8	0.8	44.50	10.71
B	0.22	0.88	0.90	48.53	11.31
C	0.22	0.87	0.95	49.37	11.58
D	0.31	0.93	0.96	52.50	13.02
E	0.34	0.96	0.96	53.77	14.50

4.2 Three-objective optimization

To further consider the influence of exergy loss of the main components on the cycle performance analysis, Fig. 11 shows the Pareto frontier curve of three-objective optimization among cycle efficiency, exergy loss of the components, and cost. As shown in Fig. 11, four typical points were labeled based on different decisions. The target values corresponding to these four points and corresponding parameter values are illustrated in Table 6. Within the selected range of the optimization parameters, the variation range of cycle efficiency and cost is consistent with that of the two-objective optimization, and the exergy loss of the components is between 1.77 and 3.7 MW.

The maximum cycle efficiency is at point IV, where the overall cost is the highest and the exergy loss is minimal. The minimum cycle efficiency is at point I, where the cost is the lowest and exergy loss is the maximum. The TOPSIS solution is point III, where the cycle efficiency is 52.15 %, the cycle cost is M\$12.76, and the exergy loss is 2.05 MW. As listed in Table 6, when the optimization parameters are the lowest, the corresponding case relates to point I. When the enthalpy efficiency is the highest and the recompression fraction is close to 0.33, the corresponding case is point IV. The TOPSIS optimal solution indicates that the HTR must maintain high enthalpy efficiency and the recompression fraction is closer to the local peak point (0.33). Meanwhile, Φ_R is the main parameter to compare the results of three-objective optimization with two-objective optimization. The TOPSIS optimal Φ_R of three-objective optimization is closer to the inflection point (0.33) than that of two-objective optimization, and the TOPSIS optimal η_{th} of three-objective optimization is larger than that of two-objective optimization. The results show that the three-objective optimization is more comprehensive due to introducing the second law of thermodynamics, and its TOPSIS optimal solution is more reasonable.

Moreover, the TOPSIS cycle efficiency solution of three-objective optimization exceeds that of two-objective optimization by 2.78%. Based on the analysis in Section 3.1, in the application of concentrated solar power, the annual CO₂ emission can be directly reduced by 0.43 Gt through this optimization improvement. The results of current study are of great significance to solve the problems of environment and energy.

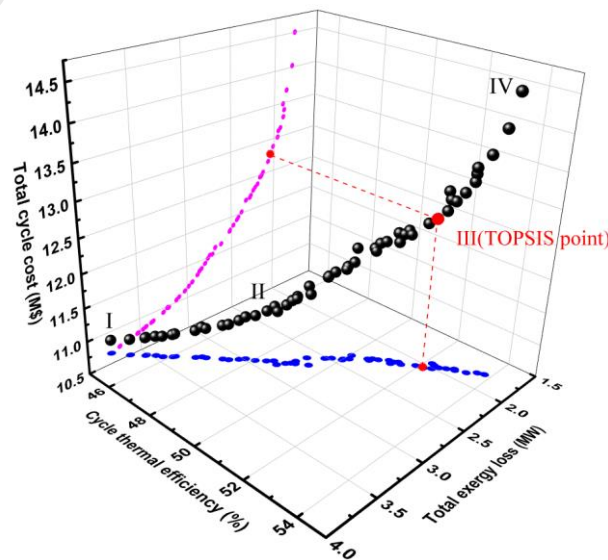


Fig. 11. Pareto frontier curve of the three-objective optimization among the cycle efficiency, total

exergy loss, and total cycle cost.

Table 6. Four typical points and corresponding parameter values with regard to the Pareto frontier of three objectives.

Point	Decision variables			Three objectives		
	Φ_R	ε_{LTR}	ε_{HTR}	$\eta_{th}(\%)$	$C_{cycle}(\text{M}\$)$	$E_{loss}(\text{MW})$
I	0.2	0.8	0.8	44.50	10.71	3.7
II	0.2	0.81	0.94	48.06	11.22	2.94
III	0.34	0.89	0.96	52.15	12.76	2.05
IV	0.34	0.96	0.96	53.77	14.50	1.77

5. Conclusions

Based on the typical SCO_2 Brayton recompression cycle process, a thermodynamic and economic mathematical model coupling the recuperator performance was developed and verified. Thermodynamic–economic analysis and multi-objective optimization were performed considering different types and designs of printed circuit recuperator. Recuperator channel types included straight, zigzag, S-shaped fins and airfoil fins. Design parameters included the ε_{LTR} , ε_{HTR} , and Φ_R . Their influences on the thermodynamic and economic performance were analyzed. Multi-objective optimization computation was carried out by adopting NSGA-II algorithm and TOPSIS method. We conclude on the following points:

(1) The correlations of Nusselt number (Nu) and Fanning friction factor (f) for the four different channel types were selected and verified with corresponding literature results, the errors were within 10%. The cycle performances of the four different recuperator channel types were contrasted with same design parameters. The combination of the LTR with a zigzag channel and HTR with a zigzag channel exhibits the best overall cycle performance when the channel hydraulic diameter is the same.

(2) The enthalpy efficiency of the recuperator and recompression fraction significantly affects cycle efficiency, cost, and exergy loss. The thermal efficiency is more sensitive to the HTR enthalpy efficiency than that of the LTR. The exergy losses of the main components are reversed. The LTR enthalpy efficiency is more sensitive to the cycle cost. There is a local inflection point of the recompression fraction ($\Phi_R=0.33$) where the cycle efficiency is maximum and exergy loss is

minimum. The total cost is the local peak value at the inflection point.

(3) Two-objective optimization considering cycle efficiency and cost was performed. The TOPSIS optimal solution was $\eta_{th}=49.37\%$, and $C_{cycle} = 11.58$ M\$. Then, the three-objective optimization considering cycle efficiency, cost, and exergy loss was conducted. The TOPSIS optimal solution is $\eta_{th}=52.15\%$, $C_{cycle}=12.76$ M\$, and $E_{loss} = 2.05$ MW. The optimal solution of three-objective considering the efficiency, total cost, and exergy loss is more comprehensive than that of two-objective optimization. In the application of concentrated solar power, the annual carbon dioxide emission can be directly reduced by 0.43 Gt through optimization efficiency improvement.

The results of the current study offer a promising route to high-efficiency and low-cost applications of SCO₂-BC by rational selection of recuperator types and designs. Moreover, the influence of recuperator types and designs on the off-design, part-load, and dynamic characteristics of SCO₂-BC will be further discussed in our future studies.

Acknowledgements

This study was supported by the CAS Project for Young Scientists in Basic Research (Grant No.YSBR-043), National Key R&D Program of China (No.2022YFB4100100), National Natural Science Foundation of China (52106117) and the Key Laboratory of Ocean Energy Utilization and Energy Conservation of Ministry of Education.

Data availability

The processing algorithm used to run simulations (as well as details on its' usage) can be found in the following Github repository: <https://github.com/linjin2016/SCO2BCthermodynamic>.

Appendix. Nomenclature

A_{cs} cross-sectional area of the channel, mm²

C cost, \$

c_p specific heat capacity, kJ·kg⁻¹·K⁻¹

D_{hy} hydraulic diameter of channel, mm

E exergy value, kW

E_L exergy loss of different components, kW

f Fanning friction factor

585	G	mass flow-flux, $\text{kg}\cdot\text{m}^{-2}\cdot\text{s}^{-1}$
586	h	specific enthalpy, kJ/kg , or convective heat transfer coefficient, $\text{kW}\cdot\text{m}^{-2}\cdot\text{K}^{-1}$
587	k	overall heat transfer coefficient, $\text{kW}\cdot\text{m}^{-2}\cdot\text{K}^{-1}$
588	KF	average heat conductance, $\text{kW}\cdot\text{K}^{-1}$
589	L	total channel length, m
590	m	mass flow-rate, $\text{kg}\cdot\text{s}^{-1}$
591	N	sub-heat exchanger element
592	Nu	Nusselt number
593	Pe	perimeter of a cross section, mm
594	Pr	Prandtl number
595	Q	heat transfer capacity, kW
596	s	specific entropy, $\text{kJ}\cdot\text{kg}^{-1}\cdot\text{K}^{-1}$
597	t	wall thickness, mm
598	T	temperature, $^{\circ}\text{C}$
599	V	volume of recuperator, m^3
600	w	specific work, $\text{kJ}\cdot\text{kg}^{-1}$
601	W	total work, kJ
602		
603		<i>Greek symbols</i>
604	δL_j	channel length of sub-element, m
605	ΔP	total pressure drop in the channel, kPa
606	δQ_{ch}	total heat transfer rate of the sub-channel unit, kW
607	ΔT_j	node temperature difference between the cold and hot streams, K
608	ε	enthalpy efficiency
609	η_c	isentropic efficiency of the compressor
610	η_{tb}	isentropic efficiency of the turbine
611	η_{th}	cycle thermal efficiency
612	λ	thermal conductivity, $\text{W}\cdot\text{m}^{-1}\cdot\text{K}^{-1}$
613	ρ	density, $\text{kg}\cdot\text{m}^{-3}$
614	Φ_R	recompression fraction
615		
616		<i>Subscripts</i>
617	af	airfoil fin
618	c	cold fluid
619	ch	channel
620	CO_2	carbon dioxide
621	$comp$	compressor
622	h	hot fluid

623 *in* inlet
 624 *isen* isentropy
 625 *m* metal material
 626 *out* outlet
 627 *PC* precooler
 628 *PHE* primary heat exchanger
 629 *r* recompressor
 630 *RC* recompression
 631 *recup* recuperator
 632 *s* S-shaped fin
 633 *st* straight channel
 634 *tb* turbine
 635 *z* zigzag channel
 636 *Abbreviations*
 637 *SCO₂* supercritical carbon dioxide
 638 *PCHE* printed circuit heat exchanger

Appendix A

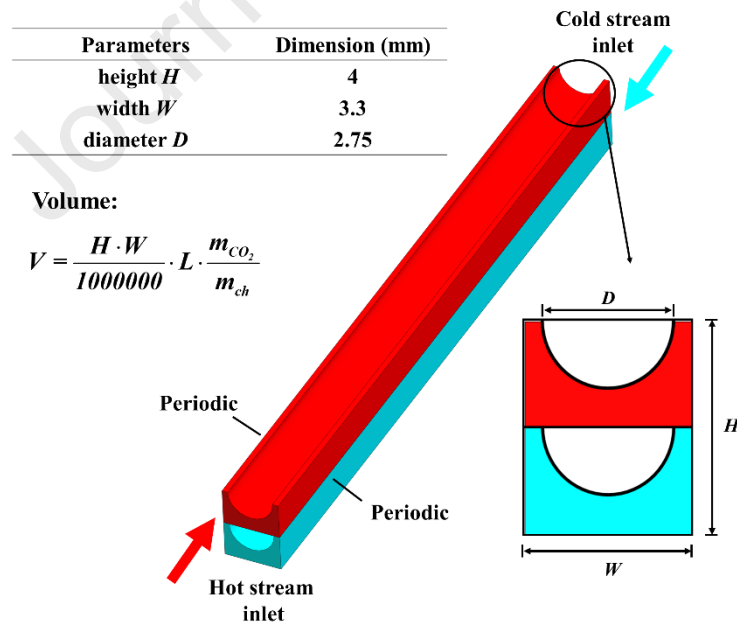
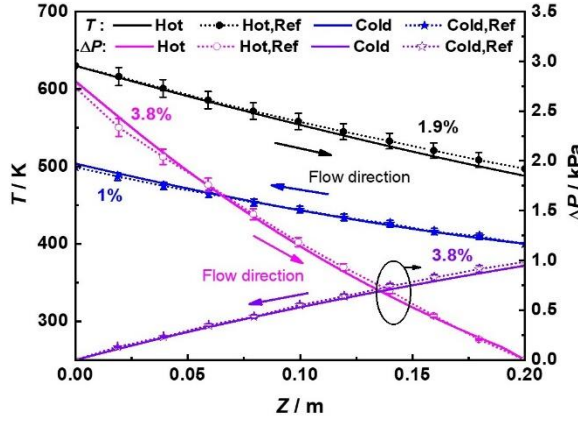


Fig. A1. Schematic diagram of a single straight PCHE unit.



Simulation condition:

$$T_{c,in}=400 \text{ K}; T_{h,in}=630 \text{ K}; P_{c,out}=22.5 \text{ MPa};$$

$$P_{h,out}=9 \text{ MPa}; m_c=0.573 \text{ g/s}; m_h=0.564 \text{ g/s};$$

length of channel $Z=200 \text{ mm}$

Correlations used in this study

$$Nu = \frac{(f_D / 8)(Re - 1000)Pr}{1 + 12.7\sqrt{f_D / 8}(Pr^{2/3} - 1)} \quad (2300 \leq Re \leq 10^6; \quad 0.6 \leq Pr \leq 10^5)$$

$$f_D = (1.82 \lg Re - 1.64)^{-2}$$

Fig. A2. Verification of the correlations between the theoretical results and simulation results for a straight PCHE.

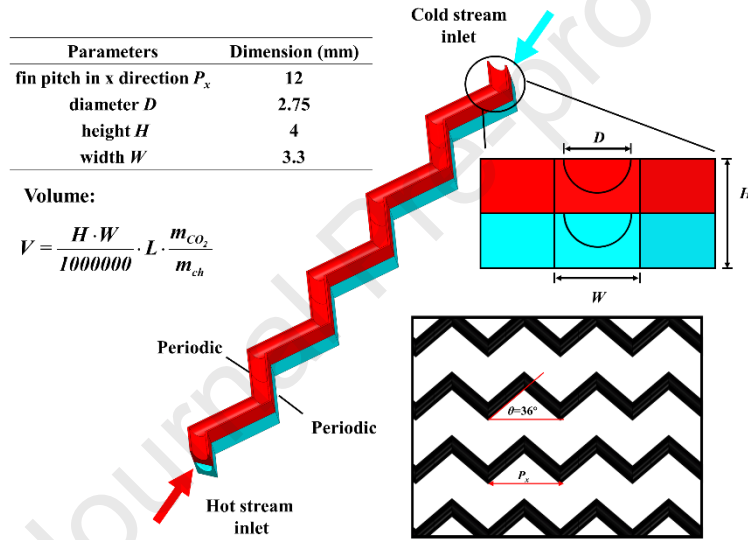
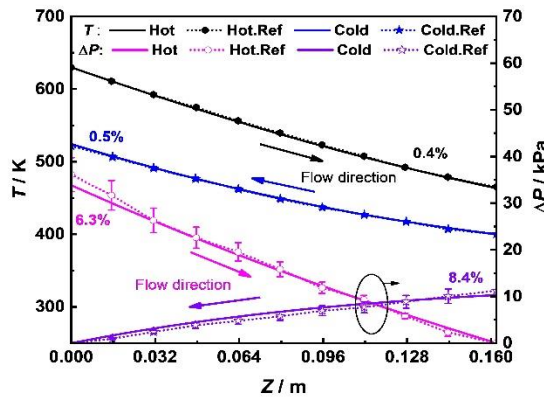


Fig. A3. Schematic diagram of a single zig PCHE unit.



Simulation condition:

$$T_{c,in}=400 \text{ K}; T_{h,in}=630 \text{ K}$$

$$P_{c,out}=22.5 \text{ MPa}; P_{h,out}=9 \text{ MPa}$$

$$m_c=0.549 \text{ g/s}; m_h=0.54 \text{ g/s}$$

$$\theta=36^\circ; P_x=12 \text{ mm}; \text{length of channel } Z=160 \text{ mm}$$

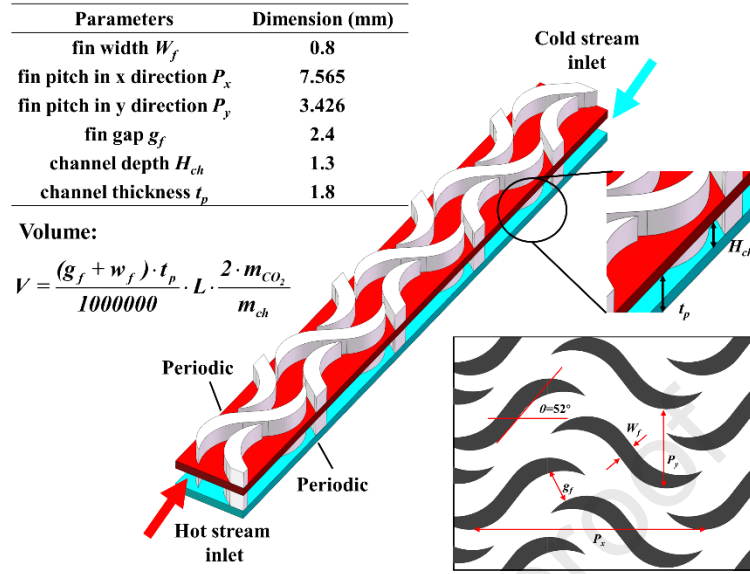
Correlations used in this study

$$Nu = 0.184 Re^{0.629} Pr^{0.317} \quad (3500 \leq Re \leq 22000; \quad 0.75 \leq Pr \leq 2.2)$$

$$f_F = 0.1924 Re^{-0.091}$$

Fig. A4. Verification of the correlations between the theoretical results and simulation results for a zigzag PCHE.

654



655

656

Fig. A5. Schematic diagram of an S-shaped fin PCHE unit.

657

Experimental conditions: length of channel is 650 mm							Comparison result			
Case	Hot side			Cold side			Case 1	Experimental results	Theoretical calculation	Error
	T_{in} (K)	P_{out} (kPa)	m (kg/s)	T_{in} (K)	P_{out} (kPa)	m (kg/s)				
1	393.57	6004.55	0.0421	321.42	10017.96	0.0246	ΔT_h	69.32 K	66.96 K	3.41%
2	393.53	5995.41	0.01435	308.13	7742.94	0.00961	ΔP_h	35.45 kPa	34.90 kPa	1.56%
							ΔT_c	63.32 K	61.20 K	3.35%
							ΔP_c	22.04 kPa	23.49 kPa	6.58%
Correlations used in this study							Case 2	Experimental results	Theoretical calculation	Error
	$Nu = 0.174 Re^{0.593} Pr^{0.43}$			(3500 $\leq Re \leq 23000$;			ΔT_h	82.5 K	80.51 K	2.41%
	$f_f = 0.4545 Re^{-0.34}$			0.75 $\leq Pr \leq 2.2$)			ΔP_h	2.59 kPa	2.85 kPa	10.0%
							ΔT_c	83.06 K	81.38 K	2.0%
							ΔP_c	7.06 kPa	7.19 kPa	1.84%

658

Fig. A6. Verification of the correlations between the theoretical results and experimental results for

660

S-shaped fin.

661

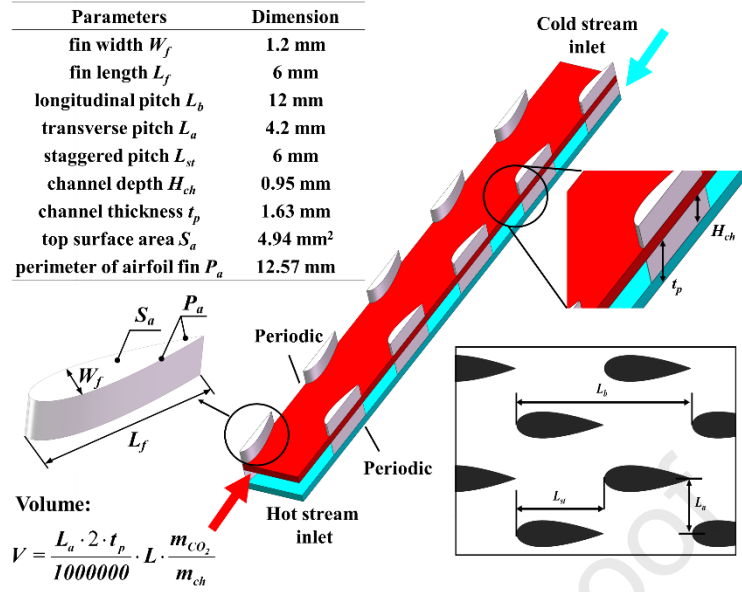


Fig. A7. Schematic diagram of an airfoil fin unit.

Simulation conditions: length of channel is 122 mm

Case	Hot side			Cold side		
	T_{in} (K)	P_{out} (MPa)	m (g/s)	T_{in} (K)	P_{out} (MPa)	m (g/s)
1	553.05	2.52	0.4335	381.05	8.28	1.8912
2	553.05	2.52	0.4335	381.05	8.28	1.4184

Comparison result

Case 1	Simulation results	Theoretical calculation	Error
Nu_c	65.89	66.78	1.3%
ΔP_c	674.15 Pa	641 Pa	4.9%
Case 2	Simulation results	Theoretical calculation	Error
Nu_c	53.39	53.13	0.5%
ΔP_c	429.6 Pa	387 Pa	9.9%

Correlations used in this study

$$Nu = 0.0318 Re^{0.78} Pr^{0.4} \quad (3000 \leq Re \leq 150000; 0.6 \leq Pr \leq 0.8)$$

$$f_D = 0.357 \left(\frac{L_b}{L_f} \right)^{-0.252} \left(\frac{W_f}{L_a} \right)^{-0.255} Re^{-0.173 \left(\frac{W_f}{L_a} \right)^{0.374}} \quad (8000 \leq Re \leq 100000)$$

Fig. A8. Verification of the correlations between the theoretical results and simulation results for an airfoil fin PCHE.

Table A1. Cycle performance with different recuperator types (L_{st} and L_z).

Performance	$L_{st}H_{st}$	$L_{st}H_z$	$L_{st}H_s$	$L_{st}H_{af}$	L_zH_{st}	L_zH_z	L_zH_s	L_zH_{af}
LTR pressure drop of cold side (kPa)	5.96	5.96	5.96	5.96	44.35	44.35	44.35	44.35
LTR pressure drop of hot side (kPa)	21.38	21.38	21.38	21.38	177.38	177.38	177.38	177.38
HTR pressure drop of cold side(kPa)	9.19	65.99	19.40	16.99	9.26	66.54	19.56	17.14
HTR pressure drop of hot side (kPa)	32.92	247.4	70.32	61.79	32.40	243.62	69.22	60.82
LTR overall heat transfer coefficient ($W \cdot m^{-2} \cdot K^{-1}$)	648.1	648.1	648.1	648.1	1005.8	1005.8	1005.8	1005.8
HTR overall heat transfer coefficient ($W \cdot m^{-2} \cdot K^{-1}$)	755.9	1194.0	778.6	954.6	756.11	1194.3	778.75	954.77

LTR Nu of cold side	38.35	38.35	38.35	38.35	63.75	63.75	63.75	63.75
HTR Nu of cold side	51.30	81.68	53.16	64.68	51.32	81.70	53.18	64.70
LTR pinch point (K)	10.36	10.36	10.36	10.36	9.56	9.56	9.56	9.56
HTR pinch point (K)	17.14	17.14	17.14	17.14	17.15	17.15	17.15	17.15
LTR volume (m ³)	2.26	2.26	2.26	2.26	1.51	1.51	1.51	1.51
HTR volume (m ³)	1.98	1.27	1.48	1.35	1.99	1.27	1.49	1.35
Cycle thermal efficiency (%)	52.44	52.43	52.44	52.44	52.55	52.54	52.55	52.55
Total cost (M\$)	14.36	13.68	13.88	13.75	13.65	12.97	13.18	13.04
Main component exergy loss (MW)	1.96	1.96	1.96	1.96	1.94	1.93	1.94	1.94

Table A2. Cycle performance with different recuperator types (L_s and L_{af}).

Performance	$L_s H_{st}$	$L_s H_z$	$L_s H_s$	$L_s H_{af}$	$L_{af} H_{st}$	$L_{af} H_z$	$L_{af} H_s$	$L_{af} H_{af}$
LTR pressure drop of cold side (kPa)	13.12	13.12	13.12	13.12	11.02	11.02	11.02	11.02
LTR pressure drop of hot side (kPa)	43.97	43.97	43.97	43.97	41.51	41.51	41.51	41.51
HTR pressure drop of cold side(kPa)	9.20	66.08	19.43	17.02	9.20	66.06	19.42	17.01
HTR pressure drop of hot side (kPa)	32.84	246.8	70.16	61.65	32.85	246.90	70.18	61.66
LTR overall heat transfer coefficient (W·m ⁻² ·K ⁻¹)	678.8	678.8	678.8	678.8	805.58	805.58	805.58	805.58
HTR overall heat transfer coefficient (W·m ⁻² ·K ⁻¹)	755.9	1194.1	778.6	954.6	755.91	1194.1	778.58	954.58
LTR Nu of cold side	44.70	44.70	44.70	44.70	47.73	47.73	47.73	47.73
HTR Nu of cold side	51.30	81.68	53.17	64.68	51.30	81.68	53.17	64.68
LTR pinch point (K)	10.24	10.24	10.24	10.24	10.26	10.26	10.26	10.26
HTR pinch point (K)	17.14	17.14	17.14	17.14	17.14	17.14	17.14	17.14
LTR volume (m ³)	1.66	1.66	1.66	1.66	1.56	1.56	1.56	1.56
HTR volume (m ³)	1.98	1.27	1.48	1.35	1.98	1.27	1.48	1.35
Cycle thermal efficiency (%)	52.46	52.44	52.45	52.45	52.45	52.44	52.45	52.45
Total cost (M\$)	13.79	13.11	13.31	13.18	13.70	13.01	13.22	13.09
Main component exergy loss (MW)	1.96	1.95	1.95	1.95	1.96	1.95	1.96	1.96

References

- 675 Ahn, Y., Bae, S.J., Kim, M., Cho, S.K., Baik, S., Lee, J.I., Cha, J.E., 2015. Review of supercritical
676 CO₂ power cycle technology and current status of research and development. Nucl. Eng. Technol.
677 47(6), 647-661. <https://doi.org/10.1016/j.net.2015.06.009>.
- 678 Al-Sulaiman, F.A., Atif, M., 2015. Performance comparison of different supercritical carbon dioxide
679 Brayton cycles integrated with a solar power tower. Energy 82, 61-71.
680 <https://doi.org/10.1016/j.energy.2014.12.070>.
- 681 Carlson, M.D., Middleton, B.M., Ho, C.K., 2017. Techno-economic comparison of solar-driven
682 SCO₂ Brayton cycles using component cost models baselined with vendor data and estimates.
683 Proceedings of the ASME 2017 11th International Conference on Energy Sustainability; ES2017-
684 3590.
- 685 Chen, M., Sun, X., Christensen, R.N., Skavdahl, I., Utgikar, V., Sabharwall, P., 2016. Pressure drop
686 and heat transfer characteristics of a high-temperature printed circuit heat exchanger. Appl. Therm.
687 Eng. 108, 1409-1417. <https://doi.org/10.1016/j.applthermaleng.2016.07.149>.
- 688 Cheng, K., Zhou, J., Huai, X., Guo, J., 2021. Experimental exergy analysis of a printed circuit heat
689 exchanger for supercritical carbon dioxide Brayton cycles. Appl. Therm. Eng. 192, 116882.
690 <https://doi.org/10.1016/j.applthermaleng.2021.116882..>
- 691 Chu, W., Li, X., Ma, T., Chen, Y., Wang, Q., 2017. Study on hydraulic and thermal performance of
692 printed circuit heat transfer surface with distributed airfoil fins. Appl. Therm. Eng. 114, 1309-1318.
693 <https://doi.org/10.1016/j.applthermaleng.2016.11.187>.
- 694 Cui, X., Guo, J., Huai, X., Cheng, K., Zhang, H., Xiang, M., 2018. Numerical study on novel airfoil
695 fins for printed circuit heat exchanger using supercritical CO₂. Int. J. Heat Mass Tran. 121, 354-
696 366. <https://doi.org/10.1016/j.ijheatmasstransfer.2018.01.015>.
- 697 Deng, T., Li, X., Zhang, L., Lian, J., Ma, T., Wang, Q., 2020. Controlling effect of phase change
698 material based heat exchanger on supercritical CO₂ Brayton cycle. J. Clean. Prod. 277, 122994.
699 <https://doi.org/10.1016/j.jclepro.2020.122994>.
- 700 Dostal, V., Hejzlar, P., Driscoll, M.J., 2006. High-performance supercritical carbon dioxide cycle
701 for next-generation nuclear reactors. Nucl. Technol. 154(3), 265-282.
702 <https://doi.org/10.13182/NT154-265>.
- 703 Dyreby, J., Klein, S., Nellis, G., Reindl, D., 2014. Design considerations for supercritical carbon
704 dioxide Brayton cycles with recompression. J. Eng. Gas Turb. Power 136(10) 101701.

- <https://doi.org/10.1115/1.4027936>.
- Dyreby, J., 2014. Modeling the supercritical carbon dioxide Brayton cycle with recompression. University of Wisconsin-Madison.
- Fleming, D., Pasch, J., Conboy, T., Carlson, M., 2013. Testing platform and commercialization plan for heat exchanging systems for SCO₂ power cycles. Proceedings of ASME Turbo Expo 2013: Turbine Technical Conference and Exposition; GT2013-95125.
- Guo, J., Li, M., He, Y., Jiang, T., Ma, T., Xu, J., Cao, F., 2022. A systematic review of supercritical carbon dioxide(S-CO₂) power cycle for energy industries: Technologies, key issues, and potential prospects. *Energy Convers. Manage.* 258, 115437. <https://doi.org/10.1016/j.enconman.2022.115437>.
- Guo, J., 2016. Design analysis of supercritical carbon dioxide recuperator. *Appl. Energ.* 164, 21-27. <https://doi.org/10.1016/j.apenergy.2015.11.049>.
- Hu, H., Liang, S., Jiang, Y., Guo, C., Guo, Y., Zhu, Y., Cai, H., 2020. Thermodynamic and exergy analysis of 2 MW S-CO₂ Brayton cycle under full/partial load operating conditions. *Energy Convers. Manage.* 211, 112786. <https://doi.org/10.1016/j.enconman.2020.112786>.
- Iverson, B.D., Conboy, T.M., Pasch, J.J., Kruienza, A.M., 2013. Supercritical CO₂ Brayton cycles for solar-thermal energy. *Appl. Energ.* 111, 957-970. <https://doi.org/10.1016/j.apenergy.2013.06.020>.
- Jin, Q., Xia, S., Li, P., Xie, T., 2022. Multi-objective performance optimization of regenerative S-CO₂ Brayton cycle based on neural network prediction. *Energy Convers. Manage.: X* 14, 100203. <https://doi.org/10.1016/j.ecmx.2022.100203>.
- Kim, D.E., Kim, M.H., Cha, J.E., Kim, S.O., 2008. Numerical investigation on thermal-hydraulic performance of new printed circuit heat exchanger model. *Nucl. Eng. Des.* 238(12), 3269-3276. <https://doi.org/10.1016/j.nucengdes.2008.08.002>.
- Kim, E.S., Oh, C.H., Sherman, S., 2008. Simplified optimum sizing and cost analysis for compact heat exchanger in VHTR. *Nucl. Eng. Des.* 238(10), 2635-2647. <https://doi.org/10.1016/j.nucengdes.2008.05.012>.
- Lemmon, E., Huber, M. and McLinden, M., 2013. NIST Standard Reference Database 23: Reference Fluid Thermodynamic and Transport Properties-REFPROP, Version 9.1. National Institute of Standards and Technology, Standard Reference Data Program, Gaithersburg, 2010.
- Li, H., Zhang, Y., Yao, M., Yang, Y., Han, W., Bai, W., 2019. Design assessment of a 5 MW fossil-

- 735 fired supercritical CO₂ power cycle pilot loop. *Energy* 174, 792-804.
 736 <https://doi.org/10.1016/j.energy.2019.02.178>.
- 737 Lian, J., Xu, D., Chang, H., Xu, Z., Lu, X., Wang, Q., Ma, T., 2021. Thermal and mechanical
 738 performance of a hybrid printed circuit heat exchanger used for supercritical carbon dioxide Brayton
 739 cycle. *Energy Convers. Manage.* 245, 114573. <https://doi.org/10.1016/j.enconman.2021.114573>.
- 740 Liu, M., Yang, K., Zhang, X., Yan, J., 2020. Design and optimization of waste heat recovery system
 741 for supercritical carbon dioxide coal-fired power plant to enhance the dust collection efficiency. *J.*
 742 *Clean. Prod.* 275, 122523. <https://doi.org/10.1016/j.jclepro.2020.122523>.
- 743 Merchán, R.P., Santos, M.J., Medina, A., Calvo Hernández, A., 2022. High temperature central
 744 tower plants for concentrated solar power: 2021 overview. *Renew. Sust. Energ. Rev.* 155, 111828.
 745 <https://doi.org/10.1016/j.rser.2021.111828>.
- 746 Meshram, A., Jaiswal, A.K., Khivsara, S.D., Ortega, J.D., Ho, C., Bapat, R., Dutta, P., 2016.
 747 Modeling and analysis of a printed circuit heat exchanger for supercritical CO₂ power cycle
 748 applications. *Appl. Therm. Eng.* 109, 861-870.
 749 <https://doi.org/10.1016/j.applthermaleng.2016.05.033>.
- 750 Neises, T., Turchi, C., 2014. A comparison of supercritical carbon dioxide power cycle
 751 configurations with an emphasis on CSP applications. *Energy Procedia* 49, 1187-1196.
 752 <https://doi.org/10.1016/j.egypro.2014.03.128>.
- 753 Ngo, T.L., Kato, Y., Nikitin, K., Ishizuka, T., 2007. Heat transfer and pressure drop correlations of
 754 microchannel heat exchangers with S-shaped and zigzag fins for carbon dioxide cycles. *Exp. Therm.*
 755 *Fluid Sci.* 32(2), 560-570. <https://doi.org/10.1016/j.expthermflusci.2007.06.006>.
- 756 Padilla, R.V., Soo Too, Y.C., Benito, R., Stein, W., 2015. Exergetic analysis of supercritical CO₂
 757 Brayton cycles integrated with solar central receivers. *Appl. Energ.* 148, 348-365.
 758 <https://doi.org/10.1016/j.apenergy.2015.03.090>.
- 759 Rao, Z., Xue, T., Huang, K., Liao, S., 2019. Multi-objective optimization of supercritical carbon
 760 dioxide recompression Brayton cycle considering printed circuit recuperator design. *Energy*
 761 *Convers. Manage.* 201, 112094. <https://doi.org/10.1016/j.enconman.2019.112094>.
- 762 Sharma, A., Shukla, A.K., Singh, O., Sharma, M., 2022. Recent advances in gas/steam power cycles
 763 for concentrating solar power. *Int. J. Ambient Energy* 43(1), 4716-4727.
 764 <https://doi.org/10.1080/01430750.2021.1919552>.

- Suzhou Zhongyan Network Technology Co. Ltd. SPSSPRO. in: www.spsspro.com.
- Tian, Y., Cheng, R., Zhang, X., Jin, Y., 2017. PlatEMO: A MATLAB platform for evolutionary multi-objective optimization [Educational Forum]. IEEE Comput. Intell. M. 12(4), 73-87. <https://doi.org/10.1109/MCI.2017.2742868>.
- Tong, Y., Duan, L., Jiang, Y., Yang, M., Pang, L., 2022. Performance study of solar tower aided supercritical CO₂ coal-fired power generation system with different schemes. Energy Convers. Manage. 252, 115113. <https://doi.org/10.1016/j.enconman.2021.115113>.
- Tsuzuki, N., Kato, Y., Ishiduka, T., 2007. High performance printed circuit heat exchanger. Appl. Therm. Eng. 27(10), 1702-1707. <https://doi.org/10.1016/j.applthermaleng.2006.07.007>.
- Utamura, M., Hasuike, H., Ogawa, K., Yamamoto, T., Fukushima, T., Watanabe, T., Himeno, T., 2012. Demonstration of supercritical CO₂ closed regenerative Brayton cycle in a bench scale experiment. ASME turbo expo 2012: turbine technical conference and exposition; p.155-64.
- Wang, K., He, Y.-L., 2017. Thermodynamic analysis and optimization of a molten salt solar power tower integrated with a recompression supercritical CO₂ Brayton cycle based on integrated modeling. Energy Convers. Manage. 135, 336-350. <https://doi.org/10.1016/j.enconman.2016.12.085>.
- Yang, J., Yang, Z., Duan, Y., 2020. Part-load performance analysis and comparison of supercritical CO₂ Brayton cycles. Energy Convers. Manage. 214, 112832. <https://doi.org/10.1016/j.enconman.2020.112832>.
- Yoon, S.H., No, H.C., Kang, G.B., 2014. Assessment of straight, zigzag, S-shape, and airfoil PCHEs for intermediate heat exchangers of HTGRs and SFRs. Nucl. Eng. Des. 270, 334-343. <https://doi.org/10.1016/j.nucengdes.2014.01.006>.
- Zhang, H., Guo, J., Cui, X., Zhou, J., Huai, X., Zhang, H., Cheng, K., Han, Z. Experimental and numerical investigations of thermal-hydraulic characteristics in a novel airfoil fin heat exchanger. Int. J. Heat Mass Tran. 2021, 175, 121333. <https://doi.org/10.1016/j.ijheatmasstransfer.2021.121333>.
- Zhao, H., Deng, Q., Huang, W., Wang, D., Feng, Z., 2016. Thermodynamic and economic analysis and multi-objective optimization of supercritical CO₂ Brayton cycles. J. Eng. Gas Turb. Power 138(8) 081602. <https://doi.org/10.1115/1.4032666>.
- Zhu, M., Zhou, J., Su, S., Xu, J., Li, A., Chen, L., Wang, Y., Hu, S., Jiang, L., Xiang, J., 2020. Study on supercritical CO₂ coal-fired boiler based on improved genetic algorithm. Energy Convers.

795 Manage. 221, 113163. <https://doi.org/10.1016/j.enconman.2020.113163>.

796

1. Printed circuit recuperator types and designs are included in recompression cycle model.
2. Thermo-economic performances are assessed with multi-objective optimization method.
3. Effects of recuperator effectiveness and recompression fraction are significant.
4. Optimal recuperator design parameters depend on the preferred objective.
5. The solution of three-objective optimization is more comprehensive than that of two-objective.

The authors declare that they have no known competing financial interests or personal relationships that could have appeared to influence the work reported in this paper.

Journal Pre-proof